

**Optimal entrainment for removal of pinned spiral waves**

Tuhin Subhra Das and Dan Wilson\*

*Department of Electrical Engineering and Computer Science, University of Tennessee, Knoxville, Tennessee 37996, USA*

(Received 7 March 2022; revised 24 May 2022; accepted 31 May 2022; published 30 June 2022)

Cardiac fibrillation is caused by self-sustaining spiral waves that occur in the myocardium, some of which can be pinned to anatomical obstacles, making them more difficult to eliminate. A small electrical stimulation is often sufficient to unpin these spirals but only if it is applied during the vulnerable unpinning window. Even if these unpinning windows can be inferred from data, when multiple pinned spirals exist, their unpinning windows will not generally overlap. Using phase-based reduction techniques, we formulate and solve an optimal control problem to yield a time-varying external voltage gradient that can synchronize a collection of spiral waves that are pinned to a collection of heterogeneous obstacles. Upon synchronization, the unpinning windows overlap so that they can be simultaneously unpinned by applying an external voltage gradient pulse at an appropriate moment. Numerical validation is presented in bidomain model simulations. Results represent a proof-of-concept illustration of the proposed unpinning strategy which explicitly incorporates heterogeneity in the problem formulation and requires no real-time feedback about the system state.

DOI: [10.1103/PhysRevE.105.064213](https://doi.org/10.1103/PhysRevE.105.064213)**I. INTRODUCTION**

Spiral waves are self-sustaining spatiotemporal patterns that can occur in many different excitable systems [1–4]. In cardiac systems, spiral waves in two-dimensional domains (and scroll waves in three dimensions [5]) give rise to cardiac arrhythmias such as tachycardia that result in an abnormally fast resting heartbeat and fibrillation that can lead to cardiac arrest [3,6–8]. The clinical standard for eliminating these arrhythmias is to apply an intense shock across the myocardium, usually requiring a voltage gradient of upwards of 5 V/cm [9]. Generally, defibrillating shocks are intensely painful, and repeated application of shocks causes additional damage to already malfunctioning hearts [10–12]. These adverse effects have motivated the search for low-energy strategies to eliminate spiral waves.

Rather than eliminating spiral waves with a single large resetting stimulus, low-energy strategies have been developed by considering spiral wave dynamics in response to inputs. Many strategies consider the dynamics of spiral waves using adjoint modes to the neutral symmetries, subsequently viewing spiral wave behavior in terms of a rigidly rotating core with spatial translation [6,13–15]. This understanding has fostered the development of antitachycardia pacing strategies [16–18] whereby traveling waves emanating from a point source can replace spirals by driving them to an inexcitable boundary. Additionally, the application of multiple low-intensity defibrillating pulses instead of one large shock has been shown to reduce the energy threshold required for successful defibrillation [19–21]. Related studies have considered simplified models in the context of developing optimized pulsing patterns [22,23]. Strategies that consider defibrillation

through the application of high-frequency electric fields have also been considered [24–26].

In realistic cardiac geometries, spiral waves have a tendency to attach or become pinned to anatomical obstacles that create tissue conductivity discontinuities such as blood vessels, anatomical defects, or cleft spaces [27–29]. These pinned spiral waves present an additional challenge in the development of low-energy defibrillation techniques; unpinned spirals are free to drift throughout the domain where they can be absorbed through inexcitable boundaries, while pinned spirals remain anchored in place. Various strategies have been proposed for unpinning spirals using target waves [30,31] or externally applied electric fields [28,32,33]. Generally, an externally applied voltage field can unpin a spiral wave but only when applied in a small window of time. Difficulties with this strategy arise when multiple pinned spirals exist simultaneously, each with a different phase relative to its unpinning window. The collection of unpinning windows is unlikely to overlap on its own, making simultaneous unpinning difficult. As suggested in [34], pacing frequencies can be determined in order to adequately scan the phase window, but it is not obvious how to generalize this strategy in situations with multiple heterogeneous pinned spirals.

In this work we consider the problem of simultaneously unpinning a large collection of spirals pinned to a heterogeneous collection of anatomical obstacles. Pinned spirals can often be characterized according to a stable periodic orbit, allowing for the use of phase-based reduction techniques [35–37] to consider the dynamics with a low-dimensional representation. Here we leverage these phase reduction techniques and implement a general strategy that can be used to identify periodic stimuli that can efficiently synchronize multiple spirals so that their unpinning windows overlap, subsequently allowing for simultaneous unpinning. We focus on implementation using a time-varying external voltage gradient as a control input.

\*Corresponding author: [dwilso81@utk.edu](mailto:dwilso81@utk.edu)

Notably, our approach explicitly allows for heterogeneity in the period and the phase response to inputs of the pinned spirals. Additionally, once an optimal entraining stimulus is found, implementation does not require any state feedback since the phase of the spirals is locked to the phase of the exogenous input.

The organization of this paper is as follows: Section II provides necessary background on numerical methods and phase-based model order reduction techniques used in this work. We also discuss the optimal control problem formulation and method of solution in the context of synchronization of a collection of heterogeneous spirals in order to align their unpinning windows. Section III presents results when considering a four-dimensional model that replicates the dynamics of human ventricular cells in conjunction with bidomain model simulations [38,39]. Section IV provides concluding remarks.

## II. NUMERICAL METHODS AND OPTIMAL CONTROL FORMULATION

### A. Numerical simulation of bidomain equations

Numerical simulations use the bidomain model, which is governed by the following equations [38,39]:

$$\begin{aligned} \nabla \cdot \bar{\sigma}_i \nabla V_i &= \beta I_m, \\ \nabla \cdot \bar{\sigma}_e \nabla V_e &= -\beta I_m, \\ I_m &= C_m \frac{\partial V_m}{\partial t} + I_{\text{ion}}, \\ V_m &= V_i - V_e. \end{aligned} \quad (1)$$

Here, intracellular and extracellular potentials are given by  $V_i$  and  $V_e$ ,  $V_m$  is the transmembrane voltage,  $C_m = 1 \mu\text{F}/\text{cm}^2$  denotes the membrane capacitance,  $\bar{\sigma}_i$  and  $\bar{\sigma}_e$  are intra- and extracellular conductivity tensors,  $\beta = 1000 \text{ cm}^{-1}$  is the surface area to volume ratio of the cell membrane, and  $\nabla$  denotes the spatial gradient. The term  $I_{\text{ion}}$  represents the cellular ionic current density and is governed by a four-dimensional model [40] that replicates the dynamics of the Ten Tusscher–Noble–Noble–Panfilov model for human ventricular myocytes [41].

The model (1) is simulated using a square domain  $\Omega$  with no current flux across the intracellular boundary so that  $\bar{\sigma}_i \nabla V_i \cdot \nu = 0$ , where  $\nu$  is a unit vector normal to the tissue boundary and the dot denotes the dot product. No flux boundary conditions are taken on the top and bottom of the extracellular domain, with a time-varying electric flux imposed on the left and right boundaries that would result from the application of an external electric field. Conductivity tensors are taken to be

$$\begin{aligned} \bar{\sigma}_i &= \begin{bmatrix} g_{ix}(x, y) & 0 \\ 0 & g_{iy}(x, y) \end{bmatrix}, \\ \bar{\sigma}_e &= \begin{bmatrix} g_{ex}(x, y) & 0 \\ 0 & g_{ey}(x, y) \end{bmatrix}, \end{aligned} \quad (2)$$

with nominal values  $g_{ex}$ ,  $g_{ey}$ ,  $g_{ix}$ , and  $g_{iy}$  equal to 0.8, 2.0 0.2, and 2.0 mS/cm, respectively. These anisotropy ratios are identical to those used in [42]. With this setup, the principle fiber direction is oriented vertically and the electric field is applied horizontally, i.e., transverse to the principle fiber direction. We

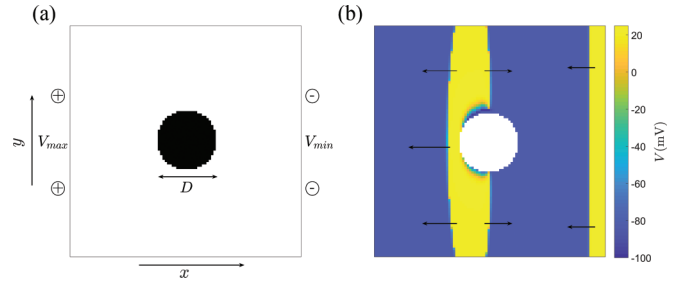


FIG. 1. Panel A shows an example domain for the bidomain model considered in this work. The domain is square with a discontinuity incorporated by setting  $g_{ix}$  and  $g_{iy}$  to zero inside a circle of diameter  $D$ . Panel B shows the result of an extracellular voltage gradient (increasing from right to left) applied for an initial condition for which all cells are quiescent. Action potentials are initiated at the left edge of the circular discontinuity and the right edge of the domain. Regions of hyperpolarization are also induced at the right edge of the circular discontinuity and the left edge of the domain during the application of the electric field, but these disappear quickly. Arrows indicate the direction of travel of the depolarization waves.

model discontinuities in the tissue by setting  $g_{ix}$  and  $g_{iy}$  to zero in a circular region at the center of the domain.

For simulation and analysis purposes, the bidomain equations (1) are typically manipulated to yield

$$\frac{\partial V_m}{\partial t} = A_i V_m + A_e V_e - I_{\text{ion}}/C_m, \quad (3)$$

subject to the constraint

$$(A_i + A_e)V_e = -A_i V_m, \quad (4)$$

where  $A_i \equiv \nabla \cdot \bar{\sigma}_i \nabla / (\beta C_m)$  and  $A_e \equiv \nabla \cdot \bar{\sigma}_e \nabla / (\beta C_m)$ . The operator splitting scheme from [43] is used to simulate Eq. (1). Simulations are performed on a  $100 \times 100$  grid using a spatial discretization of  $338 \mu\text{m}$  and a temporal discretization of 0.1 ms. The spiral dynamics are considered in the applications to follow after simulating long enough for transients to die out with solutions decaying to an underlying stable periodic orbit. Panel A of Fig. 1 highlights the geometry described above with simulations performed on the square domain with a circular discontinuity with diameter  $D$ . For the geometry considered in this work, positive (resp. negative) voltage gradients are associated with an increasing (resp. decreasing) extracellular voltage from right to left. Panel B illustrates the influence of a voltage gradient of 8.6 V/cm applied for 3 ms, starting from an initial condition for which all cells are quiescent. The discontinuity acts as a virtual electrode, and the application of the electric field elicits an action potential emanating from the left edge of the discontinuity that subsequently spreads throughout the domain. As a result of the application of this external electric field, action potentials are also initiated at the right edge of the domain.

### B. Asymptotic phase and phase reduction

The dynamics of the bidomain model equations governed by Eqs. (3) and (4) are difficult to consider directly due to their high dimensionality, complexity, and nonlinearity. Instead, the dynamics of pinned spiral waves will be

analyzed using phase reduction [35–37]. To proceed, let  $X(r, t) = [V_m(r, t) \quad s(r, t)]$  be the state with  $s \in \mathbb{R}^n$  representing a set of local auxiliary variables (gating variables, ion concentrations, etc.) that set the transmembrane current density. Here,  $r$  denotes the location on the spatial domain  $\Omega$ , with  $u(t) \in \mathbb{R}$  being the strength of the electric field. We represent the dynamics of Eq. (3) as

$$\frac{\partial X(r, t)}{\partial t} = F[X(r, t), u], \quad (5)$$

where  $F$  sets the system dynamics. Suppose that Eq. (5) admits a stable,  $T$ -periodic limit cycle  $X^\gamma(r, t)$  when taking  $u(t) = 0$ , that is, in the absence of an external electric field. For all initial conditions  $X^*$  in the basin of attraction of the periodic orbit, one can define a unique phase  $\theta(X^*) \in [0, 2\pi)$  using the notion of an asymptotic phase defined so that

$$\lim_{t \rightarrow \infty} \left| X(r, t) - X^\gamma \left( r, t + \frac{T}{2\pi} \theta(X^*) \right) \right| = 0, \quad (6)$$

where  $X(r, t)$  gives the evolution of (5) under the flow with initial condition  $X^*$  when taking  $u(t) = 0$ . Correspondingly, level sets of  $\theta$  are often referred to as isochrons [44,45]. One can verify that according to the definition (6),  $d\theta/dt = 2\pi/T \equiv \omega$  when evolved under the unperturbed flow.

For an initial condition near the stable limit cycle, one can analyze (5) using these asymptotic phase coordinates; from the chain rule, one finds

$$\begin{aligned} \frac{d\theta(X)}{dt} &= \langle \nabla \theta(X), \partial X / \partial t \rangle, \\ &= \langle \nabla \theta(X), F(X(r, t), u) \rangle, \end{aligned} \quad (7)$$

where the gradient of  $\theta$  is evaluated at the intersection of  $X^\gamma(r, t)$  and the  $\theta(X)$  isochron. In the limit that the input  $u(t)$  is small, the dynamics associated with Eq. (5) are well approximated according to

$$\frac{\partial X(r, t)}{\partial t} = F[X(r, t), 0] + \frac{\partial F}{\partial u} u(t), \quad (8)$$

where  $\partial F / \partial u$  is also evaluated at the intersection of  $X^\gamma(r, t)$  and the  $\theta(X)$  isochron. As such, Eq. (7) can be manipulated to yield

$$\begin{aligned} \frac{d\theta}{dt} &= \left\langle \nabla \theta(X), F(X(r, t), 0) + \frac{\partial F}{\partial u} u(t) \right\rangle, \\ &= \omega + \left\langle \nabla \theta(X), \frac{\partial F}{\partial u} u(t) \right\rangle, \\ &= \omega + Z(\theta) u(t). \end{aligned} \quad (9)$$

Note that in the second line above,  $\langle \nabla \theta(X), F(X(r, t), 0) \rangle = \omega$  as mandated by the definition of isochrons. In the third

line  $Z(\theta) \equiv \langle \nabla \theta(X), \partial F / \partial u \rangle$  is often referred to as a phase response curve, which captures the effect of an input applied at a particular phase of oscillation.

### C. Direct method for inference of phase response curves

In order to apply the phase reduction from Eq. (9), it is necessary to identify  $Z(\theta)$ . This can be accomplished in some situations by solving numerically for  $\nabla \theta(X)$  by finding appropriate solutions to an adjoint equation [46] (cf. [47]). In other cases it is more convenient to infer  $Z(\theta)$  using the direct method [3,48]. Given the complexity of the bidomain equations governed by Eq. (3), we will employ the direct method in this work, which is described below.

The direct method can be implemented by applying a pulse of input  $u(t) = a_0$  lasting  $t_0$  time units starting at a known phase  $\theta_0$ . From Eq. (9), the difference in phase caused by the application of the pulse input is given by  $\Delta\theta \approx Z(\theta_0) a_0 t_0$ . As such, by inferring the change in phase  $\Delta\theta$  in response to this input, a pointwise estimate of the phase response curve can be estimated according to

$$Z(\theta_0) \approx \frac{\Delta\theta}{a_0 t_0}. \quad (10)$$

By repeating this procedure for multiple choices of  $\theta_0$ ,  $Z(\theta)$  is taken to be a curve fit to the resulting data. Here,  $\Delta\theta$  can be computed following the application of the input by considering the change in oscillation timing once the pinned spiral wave relaxes back to its limit cycle.

### D. Entrainment of heterogeneous spirals using a time-varying electric flux

Consider two oscillators governed by the phase-reduced equations

$$\begin{aligned} \dot{\theta}_1 &= \omega_0 + Z(\theta_1) u(t), \\ \dot{\theta}_2 &= \omega_0 + \Delta\omega + [Z(\theta_2) + \Delta Z(\theta_2)] u(t), \end{aligned} \quad (11)$$

where  $\theta_1$  is the phase of a nominal oscillator with frequency  $\omega_0$  and phase response curve  $Z(\theta_1)$ . We also consider a second oscillator with a natural frequency that differs from the nominal by  $\Delta\omega \in [-\Delta\omega_-, \Delta\omega_+]$  and a phase response curve that differs from nominal by  $-E_-(\theta) \leq \Delta Z(\theta) \leq E_+(\theta)$ . Intuitively, oscillator 1 captures the nominal system properties and oscillator 2 accounts for uncertainty. We assume that both  $u(t)$  and  $\Delta\omega$  are order  $\epsilon$  terms where  $0 < \epsilon \ll 1$ . Defining a new variable  $\phi = \theta_2 - \theta_1$ , using Eq. (11) one finds

$$\dot{\phi} = \Delta\omega + [Z(\theta_1 + \phi) - Z(\theta_1) + \Delta Z(\theta_1 + \phi)] u(t). \quad (12)$$

Neglecting order  $\epsilon$  terms from the dynamics given in Eq. (11), one finds that  $\theta_1(t) = \theta_1(0) + \omega_0 t + O(\epsilon)$ . Substituting this result into Eq. (12) yields

$$\dot{\phi} = \Delta\omega + [Z(\omega_0 t + \phi) - Z(\omega_0 t) + \Delta Z(\omega_0 t + \phi)] u(t) + O(\epsilon^2), \quad (13)$$

where  $\theta_1(0)$  is taken to be zero for simplicity. We take  $u_0$  to be a  $T$ -periodic input with period  $T = 2\pi/\omega_0$  so that Eq. (13) is  $T$  periodic. Noting that Eq. (13) is of the general form  $\dot{v} = \epsilon Q(v, t)$ , formal averaging techniques [44,49] can be applied to

approximate (13) according to

$$\dot{\Phi} = \Delta\omega + \underbrace{\frac{1}{T} \int_0^T [Z(\omega_0 t + \Phi) - Z(\omega_0 t) + \Delta Z(\omega_0 t + \Phi)] u(t) dt}_{f(\Phi)}, \quad (14)$$

where  $\Phi$  is a good approximation for  $\phi$ . Additionally, stable fixed points of Eq. (14) correspond to stable entrained solutions of the unaveraged equations (13). Equation (14) is often referred to as a coupling function, which admits stable locked solutions for crossings of  $\dot{\Phi} = 0$  with negative slope. As explained with a graphical argument in [50], provided that the following two conditions are satisfied,

$$f(\theta_+) < -\Delta\omega_+, \quad (15)$$

$$f(-\theta_-) > \Delta\omega_-, \quad (16)$$

for some  $\theta_+$  and  $\theta_-$ , the intermediate value theorem guarantees that Eq. (14) admits a stable fixed point somewhere on the interval  $[-\Delta\theta_-, \Delta\theta_+]$ . Note that because the oscillators from Eq. (11) are not coupled, the above analysis can be applied to

population of oscillators, each with properties that fall within the range of allowable heterogeneity.

### E. Optimal control formulation and numerical solution

Ultimately, the goal is to design an optimal electric field flux  $u(t)$  that will synchronize the phase of a collection of heterogeneous pinned spirals so that their unpinning windows overlap. Specifically, we seek to identify a stimulus  $u(t)$  that satisfies the conditions (15) and (16) for a given choice of  $\theta_+$  and  $\theta_-$  and minimizes the cost functional  $C[u(t)] = \int_0^T u^2(t) dt$ . To achieve this goal, we will employ the strategy proposed in [50]. A simplified derivation of this control strategy is given here.

We start by manipulating the relations (15) and (16). One can rewrite condition (15) as

$$\frac{1}{T} \int_0^T \left[ \int_0^{\theta_+} Z'(\omega_0 t + s) u(t) ds + \Delta Z(\omega_0 t + \theta_+) u(t) \right] dt < -\Delta\omega_+, \quad (17)$$

which will be satisfied provided

$$\frac{1}{T} \int_0^T \left[ \int_0^{\theta_+} Z'(\omega_0 t + s) u(t) ds + \max_{\Delta Z} (\Delta Z(\omega_0 t + \Delta\theta_+) u(t)) \right] dt < -\Delta\omega_+. \quad (18)$$

Likewise, Eq. (16) will be satisfied provided

$$\frac{1}{T} \int_0^T \left[ \int_0^{-\theta_-} Z'(\omega_0 t + s) u(t) ds + \min_{\Delta Z} (\Delta Z(\omega_0 t - \Delta\theta_-) u(t)) \right] dt > \Delta\omega_-. \quad (19)$$

With Eqs. (18) and (19) in mind, the optimal control input can be obtained using a Hamilton-Jacobi-Bellman approach [51] by defining the system

$$\dot{y} = \begin{bmatrix} \dot{a} \\ \dot{b} \\ \dot{\theta} \end{bmatrix} = \begin{bmatrix} \frac{1}{T} \int_0^{\theta_+} Z'(\omega_0 t + s) u(t) ds + \frac{1}{T} \max_{\Delta Z} (\Delta Z(\omega_0 t + \Delta\theta_+) u(t)) \\ \frac{1}{T} \int_0^{-\theta_-} Z'(\omega_0 t + s) u(t) ds + \frac{1}{T} \min_{\Delta Z} (\Delta Z(\omega_0 t - \Delta\theta_-) u(t)) \\ \omega_0 + Z(\theta) u(t) \end{bmatrix}. \quad (20)$$

Here,  $a$  and  $b$  are auxiliary variables that correspond to constraints (18) and (19). Then the desired energy-optimal stimulus will minimize

$$J(y, u) = \int_0^T u^2 dt + q(y(T)), \quad (21)$$

where  $\int_0^T u^2 dt$  gives a sense of the power consumed by the stimulus, and  $q(y(T))$  provides a penalty for failing to reach the target set. Specifically,  $q(y(T))$  is small when the endpoint conditions  $a(T) < -\Delta\omega_+$ ,  $b(T) > \Delta\omega_-$ , and  $\theta(T) = 2\pi$  are satisfied. For final states for which these conditions are not satisfied,  $q(y(T))$  is a large penalty. A Hamilton-Jacobi-Bellman equation can be solved to obtain the cost-to-go

function (also known as the value function)

$$\mathcal{V}(y, \tau) = \inf_{\substack{u_{\min} \leq u(t) \leq u_{\max} \\ \forall t \in [\tau, T]}} \left[ \int_{\tau}^T u^2 dt + q(y(T)) \right], \quad (22)$$

and the optimal control at a given moment in time can be obtained as the minimal solution to the Hamiltonian,

$$\mathcal{H}(y, \nabla \mathcal{V}, u) = u^2(t) + [\nabla \mathcal{V}(y(t), t)]^T \dot{y}, \quad (23)$$

subject to the allowable constraints. Subsequently, the full optimal control over the interval  $t \in [0, T]$  can be identified by solving (20) using the optimal input with initial condition  $y(0) = [0, 0, 0]$ . More details about this optimal control formulation and solution can be found in [50]. Intuitively, this optimal control framework tends to yield inputs that are

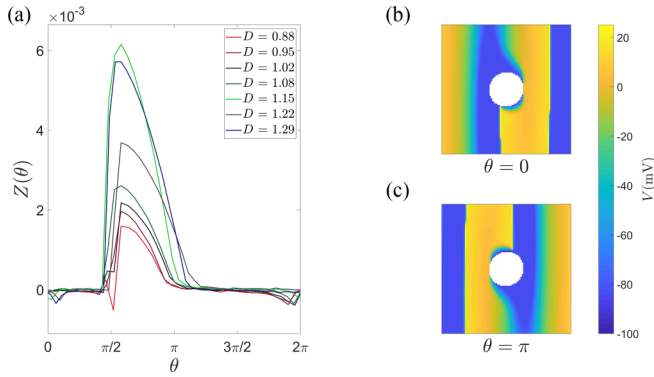


FIG. 2. Phase response curves (in units of rad cm/V s) for spirals pinned to discontinuities of various diameters,  $D$  (in cm). The phase of each spiral is most sensitive to inputs occurring between  $\theta \in [1.5, 3.8]$  with significant variation in the amplitudes of the phase response curves depending on the size of the discontinuity. Panels B and C show snapshots corresponding to phases of  $\theta = 0$  and  $\theta = \pi$ , respectively, for a discontinuity  $D = 0.88$  cm. The phases are most sensitive to input when the spiral tip is near the left side of the discontinuity, i.e., the depolarizing side of the virtual electrode that results when a positive voltage gradient is applied.

larger in magnitude when the slopes of the allowable phase response curves are simultaneously large in magnitude. In regions where there is a large amount of allowable heterogeneity or when the slopes are small in magnitude, the resulting control input is usually close to zero.

### III. RESULTS

We consider the bidomain model governed by Eqs. (3) and (4) in the presence of circular discontinuities with size ranging from  $D = 0.88$  to  $D = 1.29$  cm in diameter. Each of these configurations supports a single spiral with a period ranging from 317 to 414 ms in steady state. For each pinned spiral,  $\theta = 0$  (resp.,  $\theta = \pi$ ) corresponds to a moment when the spiral is near the bottom (resp. top) of the obstacle (for instance, see panels B and C of Fig. 2). Phase response curves are obtained by applying a voltage gradient of 2.6 V/cm lasting 9.6 ms, measuring the resulting phase difference, inferring the resulting shift in phase caused by the pulse, and using Eq. (10) to provide an estimate of the phase response curve. This process is repeated for various initial phases to obtain pointwise estimates of each phase response curve. Panel A of Fig. 2 shows resulting phase response curves associated with discontinuities of different sizes. The phase is only sensitive to inputs for  $\theta \in [1.5, 3.8]$  near the moment that the tip of the spiral wave crosses the left side of the discontinuity (corresponding to the depolarizing end of the virtual electrode induced by a positive voltage gradient). Beyond this range an applied voltage gradient does little to influence the phase. Additionally, the size of the phase response curve increases with increasing diameter of the discontinuity. This result is likely related to two different factors. First, as noted in [46], phase sensitivity functions associated with pinned spirals are concentrated near the discontinuity. Second, as observed in Fig. 5 of [19], the influence of an electric field near a discontinuity grows with its size, e.g., with larger discontinuities serving

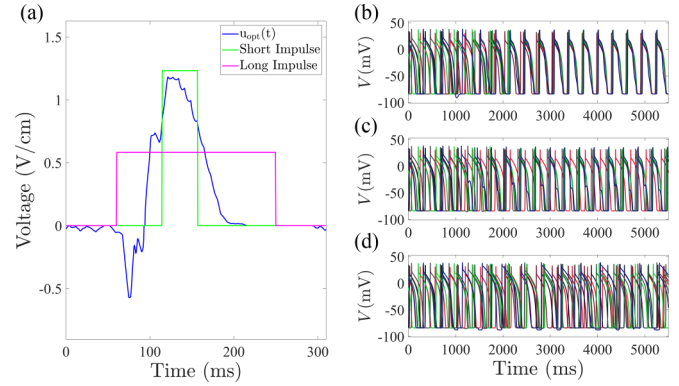


FIG. 3. Using the envelope obtained from the phase response curves from Fig. 2, the optimal control problem is formulated as described in Sec. II E and solved to yield an energy-optimal stimulus. This periodic stimulus is shown in panel A along with two comparison stimuli which represent short and long impulses with magnitudes chosen so that  $\int_0^T u^2 dt$  is identical for each stimulus. Panels B, C, and D show representative traces of transmembrane voltage when the optimal, short-impulse, and long-impulse periodic stimuli are applied to pinned spirals. The different colors represent traces from spirals pinned to discontinuities of different allowable sizes. The optimal stimulus results in tight synchronization after approximately 3000 ms. The other stimuli are unable to synchronize the phases of all spirals.

as virtual electrodes for weaker electric field strengths. These factors ultimately translate to an increase in the magnitude of the PRC as the size of the discontinuity increases.

The PRCs from Fig. 2 are used to determine the envelope  $\Delta Z$  in the optimal entrainment strategy described in Secs. II D and II E. We take  $\omega_0 = 0.0203$  rad/ms, corresponding to an entrained period of 310 ms. Compared to the unforced spiral periods, the entrained period is relatively short. This is because the spiral with the fastest period (i.e., with  $D = 0.88$  cm) is the least sensitive to input, as illustrated in Fig. 2. We also take  $\theta_+ = \theta_- = 0.63$  radians so that upon entrainment the phase of each spiral will be within 1.26 radians, allowing for some overlap in the unpinning windows. The absolute maximum value of the control input is taken to be 1.8 V/cm. The resulting optimal input is shown in blue in panel A of Fig. 3. For reference, the green and magenta lines show large- and small-magnitude pulse inputs for which  $\int_0^T u^2 dt$  are identical to the optimal input. The response to these periodic inputs is shown in panels B–D where each trace shows the transmembrane voltage at  $(x, y) = (1, 2)$  cm for spirals with discontinuities of different allowable sizes. Panel B shows results when using the optimal stimulus. The response to the comparison periodic inputs shown in green and magenta in panel A are shown in panels C and D, respectively. Note that each simulation considers a single spiral wave on a  $3.38 \times 3.38$  cm domain in response to the indicated input, and the voltage traces for each trial are superimposed. The optimal stimulus tightly synchronizes the behavior of each of the spiral waves (shown in panel B) after approximately ten cycles. Synchronization is not achieved by the comparison stimuli (panels C and D).

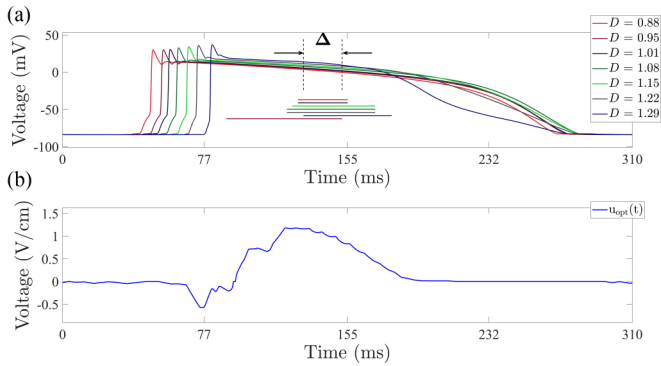


FIG. 4. In panel A, unpinning windows for spirals pinned to circular obstacles of varying diameter (in cm) are shown as horizontal lines. The colored lines show representative transmembrane voltage traces from individual spirals taken at  $(x, y) = (1, 2)$  cm after the spirals have been entrained to the optimal stimulus. Unpinning windows for the individual spirals are determined by first applying the optimal stimulus shown in Fig. 3 until the spiral is fully entrained, subsequently applying a voltage gradient of 8.6 V/cm lasting 3 ms, recording whether the spiral is unpinned from the discontinuity, and repeating this procedure for an adequate sampling of pulse timings. The timing of these pulses is shown relative to the timing of the entraining stimulus shown for reference in panel B. The overlap in the unpinning windows is denoted by  $\Delta$ . This window occurs slightly after the optimal stimulus reaches its maximum value.

We also investigate the size of the unpinning window for the spirals entrained by the energy-optimal stimulus with results shown in Fig. 4. In panel A, each color trace shows the transmembrane voltage at  $(x, y) = (2, 1)$  from a single spiral once it is entrained to the optimal stimulus. Numerically, we determine each unpinning window by applying a short duration voltage gradient of 8.6 V/cm lasting 3 ms. In these simulations, once the spiral is unpinned it is absorbed through the tissue boundary and subsequently eliminated. For larger domains, an unpinned spiral would not necessarily be absorbed by the tissue boundary because it would have more room to meander. Horizontal lines in panel A of Fig. 4 indicate the unpinning window, i.e., the time that the electric field can be applied so that the spiral will subsequently be unpinned. Because these spirals are entrained to the external voltage field, these unpinning windows are shown relative to the timing of the optimal stimulus shown for reference in panel B. This simultaneous unpinning window is close to the moment that the magnitude of the optimal input from Fig. 3 is largest. Note that this unpinning window for each individual spiral is relatively small with a minimum window of 27 ms for the spiral pinned to the  $D = 0.88$  cm discontinuity. Nonetheless, the optimal stimulus is able to sufficiently synchronize the spirals so that the unpinning windows overlap.

Representative examples of successful and unsuccessful unpinning are shown in panels A–F and G–L of Fig. 5, respectively. For a spiral pinned to a discontinuity with diameter  $D = 0.88$  cm, a short-duration voltage gradient is applied inside the pinning window with timing denoted by the black arrow in panel A. The transmembrane voltage immediately before the application of the pulse is shown in panel B. Regions of depolarization begin to emerge on the left side of the

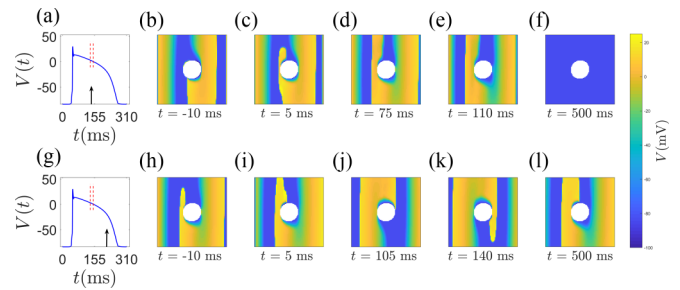


FIG. 5. Panels A–F (resp., G–L) show representative simulations for voltage gradient pulses applied inside (resp., outside) of the unpinning window. For each simulation, the spiral is first fully entrained to the optimal stimulus shown in Fig. 3. Panels A and G highlight the unpinning window illustrated in Fig. 4 for reference. The black arrows denote the timing of the application of the voltage gradient pulse. For the stimulus applied inside the unpinning window, a wave front is created at the left end of the discontinuity, which ultimately runs into the refractory tail of the preceding wave, thereby stopping wave propagation. Snapshots of the transmembrane voltage are shown in panels B–F; the timing of each snapshot given is relative to the application of the voltage gradient pulse. For the stimulus applied outside of the unpinning window, the pulse does not substantially influence the timing of the spiral wave, and the wave persists indefinitely. Because we are considering a small domain ( $3.38 \text{ cm} \times 3.38 \text{ cm}$ ), the unpinned spiral is absorbed through the tissue boundary. For a larger domain, an unpinned spiral could persist and begin to meander.

discontinuity after the pulse is applied in panel C. In panel D, the resulting wave front runs into the refractory tail of the spiral wave, stopping wave propagation. Ultimately, the spiral is absorbed by the tissue boundary, leading to quiescence 500 ms after the application of the voltage gradient pulse, as shown in panels D–F. In panels G–L, the same voltage gradient pulse is applied outside of the unpinning window. Panels H and I show the state of the spiral wave immediately before and after the pulse is applied. This pulse occurs once the spiral wave tip has already reached the left end of the discontinuity and the subsequent influence on the phase of the spiral is diminished. Panels J–L illustrate that the spiral continues to persist after the application of the voltage gradient pulse.

Figure 6 shows unpinning results for spirals pinned to discontinuities of various sizes. Panels A–D, E–H, I–L, and M–P show results from independent simulations that receive identical inputs. Spirals are initially out of phase 3375 ms prior to the application of the unpinning pulse. The optimal entraining stimulus is applied in each simulation for 3375 ms to synchronize the phase of each of the spirals. At  $t = 0$ , a voltage gradient pulse is applied inside the unpinning window of the synchronized collection of spirals. For each simulation, the resulting wave front runs into the tail of the preceding wave and is eliminated. Note that while these results come from independent simulations, they could also represent the behavior of a collection of uncoupled pinned spirals on a larger domain.

Finally, we consider the simultaneous unpinning of multiple spirals on a larger  $6.76 \times 6.76$  cm domain. On this domain, four circular discontinuities with diameter of either  $D = 0.88$  cm or  $D = 1.29$  cm are considered, as denoted by

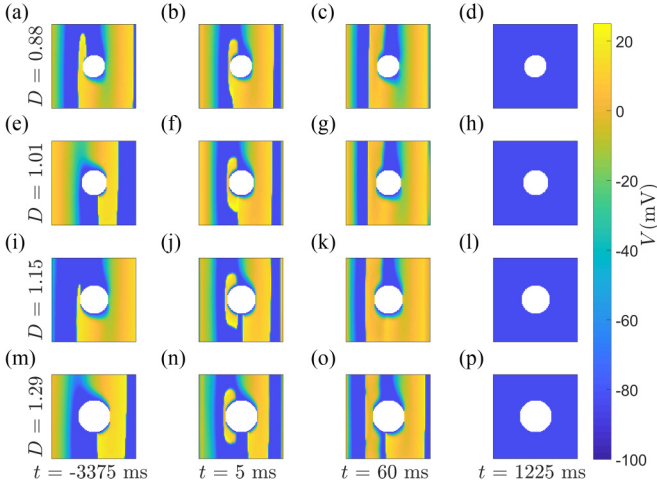


FIG. 6. Panels A–D, E–H, I–L, and M–P show results from independent simulations that receive identical inputs. Spirals are pinned to obstacles of different sizes. As such, the spiral periods and phase response curves are different. The times in each of the panels are given relative to the application of the unpinning voltage gradient pulse. Initially, the phases of each of the spirals are not aligned at  $t = -3375$  ms. The optimal entraining stimulus is subsequently applied to synchronize the phases before the application of a voltage gradient pulse at  $t = 0$  that is inside the unpinning window. The resulting wave front from the left end of the obstacle runs into the refractory tail of the preceding wave causing the spiral wave to die out.

the white dots in panels C–F of Fig. 7. This domain is large enough to support four spiral waves, each pinned to one of the four discontinuities. Here we employ the same strategy used in Fig. 6 to unpin and eliminate these spirals, i.e., by first applying the optimal entraining stimulus for approximately 3000 ms and subsequently applying a larger pulse aligned with the unpinning window. Panel B shows the applied voltage

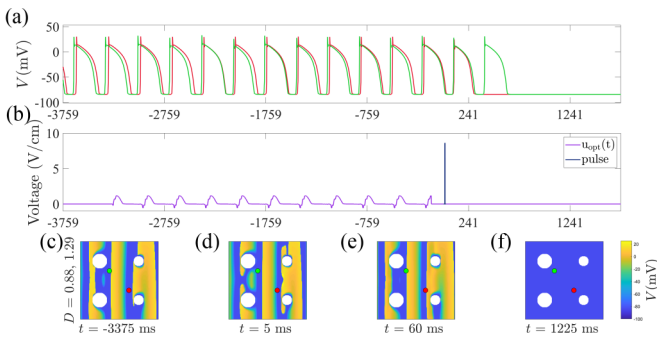


FIG. 7. Entrainment and subsequent unpinning of four pinned spirals attached to discontinuities of different sizes. These simulations are similar to those from Fig. 6, except here the spiral waves are not independent from one another. Panel A shows the transmembrane voltages of two representative points near the top-left and bottom-right spirals at locations indicated by dots of corresponding color in panels C–F. Panel B shows the applied voltage gradient. Snapshots of the transmembrane voltage are shown in panels C–F; the timing of each snapshot given is relative to the application of the voltage gradient pulse.

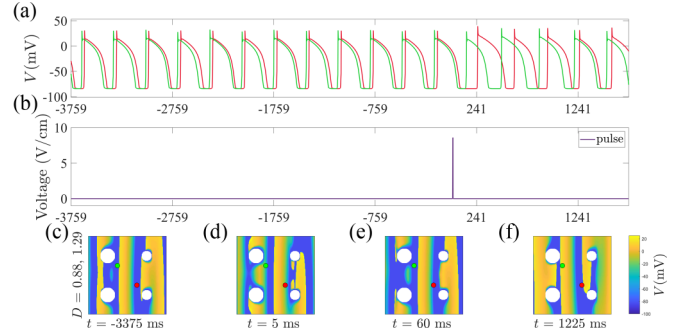


FIG. 8. Application of a short pulse without first applying an entraining stimulus in a simulation with multiple spirals. Panel A shows the transmembrane voltages of two representative points near the top-left and bottom-right spirals at locations indicated by dots of corresponding color in panels C–F. Panel B shows the applied voltage gradient. Snapshots of the transmembrane voltage are shown in panels C–F. The voltage gradient pulse applied at  $t = 0$  ms does not unpin the spirals.

gradient, and panel A shows the transmembrane voltages of two representative points near the top-left and bottom-right spirals indicated by dots of corresponding color in panels C–F. Panel C shows the state immediately before the entraining stimulus is applied. Panel D shows the state immediately after the application of the unpinning pulse. In panel E, spiral wave front propagation has ceased with the spiral wave fronts absorbed by the refractory parts of the domain. This ultimately leads to quiescence in panel F. A nearly identical simulation is shown in Fig. 8; in this case the optimal entraining stimulus is not applied but the pulse input still occurs at  $t = 0$  ms. Once again, representative voltage traces are shown in panel A with the applied voltage gradient shown in panel B. Panel C from this simulation is identical to panel C from Fig. 7. Without first applying the entraining stimulus, the pulse input does not eliminate the spiral waves, as illustrated by the snapshots from panels D–F.

#### IV. DISCUSSION AND CONCLUSION

In this work we leverage phase-based reduction techniques to investigate an energy-optimal strategy to synchronize the behavior of a set of spiral waves that are pinned to a heterogeneous collection of anatomical obstacles. This low-energy electric field is designed so that upon entrainment, the unpinning windows [28,32,33] of each spiral will overlap, allowing for simultaneous unpinning with a single pulse. Because the spirals become phase locked to the externally applied stimulus, no explicit information about the phase of each spiral is necessary. Rather, the unpinning pulse can be timed in relation to the phase of the entraining stimulus. This method is illustrated in a bidomain model (1) with the ionic currents governed by a four-dimensional model [40] that captures the important characteristics of human ventricular myocytes. Resulting optimal stimuli are able to simultaneously entrain a collection of spirals with substantially different phase response curves and natural frequencies so that they can be subsequently be unpinning. Note that in this study, we only

considered electric fields applied perpendicular to the fiber direction. Other orientations would result in different phase response curves but could readily be considered using the proposed approach.

The proposed strategy explicitly takes heterogeneity into account, thereby yielding a stimulus that can entrain a collection of pinned spirals with varied properties. This can be particularly useful in situations where phase response curves cannot be directly measured, for instance, in an experimental setting when the data collection required for implementation of the direct method might be prohibitive. In these instances an optimal entraining stimulus could still be designed if the properties of the phase models (9) associated with a collection of pinned spirals can be expected to fall within some prespecified window. A similar approach was considered in [52] in the consideration of entrained neural oscillations.

This study presents a proof of concept illustrating that a time-varying an external electric field could be used to synchronize the phase of a heterogeneous collection of pinned spirals so that they can be subsequently unpinned with a stronger pulse. We do not explicitly consider subsequent elimination strategies once the spirals are unpinned. The proposed strategy could be used in conjunction with other previously proposed low-energy spiral wave elimination strategies. For instance, [53] considers resonant drift pacing strategy where low-energy shocks are applied at the period of a given spiral wave in order to promote spiral wave drift and subsequent elimination by absorption through an inexcitable obstacle. Antitachycardia pacing strategies [16–18] can also be used to drive unpinned spirals to an inexcitable tissue boundary. An understanding of the adjoint modes associated with spatial translation [6,13–15] could also be useful for designing inputs to appropriately guide unpinned spirals to locations where they can be eliminated.

There are many limitations of the present study with a number of questions left to address. Foremost, in this study we only consider pinned spirals on a simple two-dimensional domain with circular discontinuities. We have not taken a realistic three-dimensional structure of the heart into account and have not considered realistic geometries of pinned spiral waves. These issues would certainly have an influence on the phase response properties of the resulting phase-reduced models of the form (9). The present study assumes that forced behavior of the pinned spirals are well approximated by the phase-reduced equations of the form (9). This approximation requires that the state rapidly converges to an underlying stable periodic orbit and does not allow for the consideration of memory-based effects [54,55] due to pacing history. Such effects may be important to consider for models with more realistic ionic dynamics which would need to be considered using phase-amplitude-reduced equations [56–58]. Additionally, we do not explicitly consider coupling between pinned spirals throughout the domain. While simulations shown in Fig. 7 illustrate that coupled spiral waves can still be entrained and unpinned using the proposed strategy, it would be of interest to consider the issue of coupling more carefully. This could be accomplished, for instance, by considering phase sensitivity functions described in [46] in the context of general reaction-diffusion systems. Given these limitations, we emphasize that the present study represents a proof of concept of the proposed spiral wave synchronization and subsequent elimination strategy; further investigation in more realistic models and experimental preparations would be warranted.

#### ACKNOWLEDGMENT

This material is based upon work supported by the National Science Foundation through Grant No. CMMI-1933583.

- 
- [1] S. Jakubith, H. H. Rotermund, W. Engel, A. Von Oertzen, and G. Ertl, Spatiotemporal Concentration Patterns in a Surface Reaction: Propagating and Standing Waves, Rotating Spirals, and Turbulence, *Phys. Rev. Lett.* **65**, 3013 (1990).
  - [2] A. T. Winfree, Spiral waves of chemical activity, *Science* **175**, 634 (1972).
  - [3] A. Winfree, *The Geometry of Biological Time*, 2nd ed. (Springer Verlag, New York, 2001).
  - [4] A. S. Mikhailov and K. Showalter, Control of waves, patterns and turbulence in chemical systems, *Phys. Rep.* **425**, 79 (2006).
  - [5] S. Alonso, F. Sagués, and A. S. Mikhailov, Taming Winfree turbulence of scroll waves in excitable media, *Science* **299**, 1722 (2003).
  - [6] F. Fenton, E. Cherry, H. Hastings, and S. Evans, Multiple mechanisms of spiral wave breakup in a model of cardiac electrical activity, *Chaos* **12**, 852 (2002).
  - [7] E. M. Cherry and F. H. Fenton, Visualization of spiral and scroll waves in simulated and experimental cardiac tissue, *New J. Phys.* **10**, 125016 (2008).
  - [8] Z. Qu, Chaos in the genesis and maintenance of cardiac arrhythmias, *Prog. Biophys. Mol. Biol.* **105**, 247 (2011).
  - [9] R. E. Ideker, X. Zhou, and S. B. Knisley, Correlation among fibrillation, defibrillation, and cardiac pacing, *Pacing and Clinical Electrophysiology* **18**, 512 (1995).
  - [10] G. P. Walcott, C. R. Killingsworth, and R. E. Ideker, Do clinically relevant transthoracic defibrillation energies cause myocardial damage and dysfunction? *Resuscitation* **59**, 59 (2003).
  - [11] A. Epstein, G. Kay, V. Plumb, S. Dailey, and P. Anderson, Gross and macroscopic pathological changes associated with nonthoracotomy implantable defibrillator leads, *Circulation* **98**, 1517 (1998).
  - [12] J. A. Joglar, D. J. Kessler, P. J. Welch, J. H. Keffer, M. E. Jessen, M. H. Hamdan, and R. L. Page, Effects of repeated electrical defibrillations on cardiac troponin I levels, *Am. J. Cardiol.* **83**, 270 (1999).
  - [13] B. Sandstede, A. Scheel, and C. Wulff, Dynamics of spiral waves on unbounded domains using center-manifold reductions, *J. Differ. Equations* **141**, 122 (1997).
  - [14] D. Barkley, Euclidean Symmetry and the Dynamics of Rotating Spiral Waves, *Phys. Rev. Lett.* **72**, 164 (1994).
  - [15] C. D. Marcotte and R. O. Grigoriev, Adjoint eigenfunctions of temporally recurrent single-spiral solutions in

- a simple model of atrial fibrillation, *Chaos* **26**, 093107 (2016).
- [16] M. S. Wathen, P. J. DeGroot, M. O. Sweeney, A. J. Stark, M. F. Otterness, W. O. Adkisson, R. C. Canby, K. Khalighi, C. Machado, D. S. Rubenstein, and K. J. Volosin, Prospective randomized multicenter trial of empirical antitachycardia pacing versus shocks for spontaneous rapid ventricular tachycardia in patients with implantable cardioverter-defibrillators pacing fast ventricular tachycardia reduces shock therapies (PainFREE Rx II) trial results, *Circulation* **110**, 2591 (2004).
- [17] M. S. Wathen, M. O. Sweeney, P. J. DeGroot, A. J. Stark, J. L. Koehler, M. B. Chisner, C. Machado, and W. O. Adkisson, Shock reduction using antitachycardia pacing for spontaneous rapid ventricular tachycardia in patients with coronary artery disease, *Circulation* **104**, 796 (2001).
- [18] M. O. Sweeney, Antitachycardia pacing for ventricular tachycardia using implantable cardioverter defibrillators: Substrates, methods, and clinical experience, *Pacing and Clinical Electrophysiology* **27**, 1292 (2004).
- [19] F. H. Fenton Jr., S. Luther, E. M. Cherry, N. F. Otani, V. Krinsky, A. Pumir, E. Bodenschatz, and R. F. Gilmour Jr., Termination of atrial fibrillation using pulsed low-energy far-field stimulation, *Circulation* **120**, 467 (2009).
- [20] S. Luther Jr., F. H. Fenton, B. G. Kornreich, A. Squires, P. Bittihn, D. Hornung, M. Zabel, J. Flanders, A. Gladuli, L. Campoy, E. M. Cherry, G. Luther, G. Hasenfuss, V. I. Krinsky, A. Pumir, R. F. Gilmour Jr., and E. Bodenschatz, Low-energy control of electrical turbulence in the heart, *Nature (London)* **475**, 235 (2011).
- [21] Y. C. Ji, I. Uzelac, N. Otani, S. Luther, R. F. Gilmour Jr., E. M. Cherry, and F. H. Fenton, Synchronization as a mechanism for low-energy anti-fibrillation pacing, *Heart Rhythm* **14**, 1254 (2017).
- [22] N. DeTal and F. Fenton, Optimizing low-energy anti-fibrillation pacing: Lessons from a cellular automaton model, [arXiv:2109.10861](https://arxiv.org/abs/2109.10861).
- [23] D. Wilson and J. Moehlis, Toward a more efficient implementation of antifibrillation pacing, *PLoS One* **11**, e0158239 (2016).
- [24] H. Tandri, S. H. Weinberg, K. C. Chang, R. Zhu, N. A. Trayanova, L. Tung, and R. D. Berger, Reversible cardiac conduction block and defibrillation with high-frequency electric field, *Sci. Transl. Med.* **3**, 102ra96 (2011).
- [25] S. H. Weinberg, K. C. Chang, R. Zhu, H. Tandri, R. D. Berger, N. A. Trayanova, and L. Tung, Defibrillation success with high frequency electric fields is related to degree and location of conduction block, *Heart Rhythm* **10**, 740 (2013).
- [26] D. Wilson, Stabilization of weakly unstable fixed points as a common dynamical mechanism of high-frequency electrical stimulation, *Sci. Rep.* **10**, 1 (2020).
- [27] D. Pazó, L. Kramer, A. Pumir, S. Kanani, I. Efimov, and V. Krinsky, Pinning Force in Active Media, *Phys. Rev. Lett.* **93**, 168303 (2004).
- [28] S. Takagi, A. Pumir, D. Pazo, I. Efimov, V. Nikolski, and V. Krinsky, Unpinning and Removal of a Rotating Wave in Cardiac Muscle, *Phys. Rev. Lett.* **93**, 058101 (2004).
- [29] Z. Y. Lim, B. Maskara, F. Aguel, R. Emokpae, and L. Tung, Spiral wave attachment to millimeter-sized obstacles, *Circulation* **114**, 2113 (2006).
- [30] A. Isomura, M. Hörning, K. Agladze, and K. Yoshikawa, Eliminating spiral waves pinned to an anatomical obstacle in cardiac myocytes by high-frequency stimuli, *Phys. Rev. E* **78**, 066216 (2008).
- [31] Y. Q. Fu, H. Zhang, Z. Cao, B. Zheng, and G. Hu, Removal of a pinned spiral by generating target waves with a localized stimulus, *Phys. Rev. E* **72**, 046206 (2005).
- [32] X. Feng, X. Gao, D. B. Pan, B. W. Li, and H. Zhang, Unpinning of rotating spiral waves in cardiac tissues by circularly polarized electric fields, *Sci. Rep.* **4**, 4831 (2015).
- [33] P. Bittihn, A. Squires, G. Luther, E. Bodenschatz, V. Krinsky, U. Parlitz, and S. Luther, Phase-resolved analysis of the susceptibility of pinned spiral waves to far-field pacing in a two-dimensional model of excitable media, *Philos. Trans. R. Soc. London A* **368**, 2221 (2010).
- [34] T. K. Shajahan, S. Berg, S. Luther, V. Krinski, and P. Bittihn, Scanning and resetting the phase of a pinned spiral wave using periodic far field pulses, *New J. Phys.* **18**, 043012 (2016).
- [35] Y. Kuramoto, *Chemical Oscillations, Waves, and Turbulence* (Springer-Verlag, Berlin, 1984).
- [36] E. M. Izhikevich, *Dynamical Systems in Neuroscience: The Geometry of Excitability and Bursting* (MIT Press, London, 2007).
- [37] G. B. Ermentrout and D. H. Terman, *Mathematical Foundations of Neuroscience* (Springer, New York, 2010), Vol. 35.
- [38] E. J. Vigmond, R. Weber dos Santos, A. J. Prassl, M. Deo, and G. Plank, Solvers for the cardiac bidomain equations, *Prog. Biophys. Mol. Biol.* **96**, 3 (2008).
- [39] N. Trayanova and G. Plank, Bidomain model of defibrillation, in *Cardiac Bioelectric Therapy* (Springer, Berlin, 2009), pp. 85–109.
- [40] A. Bueno-Orovio, E. M. Cherry, and F. H. Fenton, Minimal model for human ventricular action potentials in tissue, *J. Theor. Biol.* **253**, 544 (2008).
- [41] K. H. W. J. ten Tusscher, D. Noble, P. J. Noble, and A. V. Panfilov, A model for human ventricular tissue, *Am. J. Physiol.* **286**, H1573 (2004).
- [42] B. J. Roth, Electrical conductivity values used with the bidomain model of cardiac tissue, *IEEE Trans. Biomed. Eng.* **44**, 326 (1997).
- [43] J. P. Keener and K. Bogar, A numerical method for the solution of the bidomain equations in cardiac tissue, *Chaos* **8**, 234 (1998).
- [44] J. Guckenheimer, Isochrons and phaseless sets, *J. Math. Biol.* **1**, 259 (1975).
- [45] A. T. Winfree, Patterns of phase compromise in biological cycles, *J. Math. Biol.* **1**, 73 (1974).
- [46] H. Nakao, T. Yanagita, and Y. Kawamura, Phase-Reduction Approach to Synchronization of Spatiotemporal Rhythms in Reaction-Diffusion Systems, *Phys. Rev. X* **4**, 021032 (2014).
- [47] E. Brown, J. Moehlis, and P. Holmes, On the phase reduction and response dynamics of neural oscillator populations, *Neural Comput.* **16**, 673 (2004).
- [48] T. Netoff, M. A. Schwemmer, and T. J. Lewis, Experimentally estimating phase response curves of neurons: Theoretical and practical issues, in *Phase Response Curves in Neuroscience* (Springer, New York, 2012), pp. 95–129.
- [49] J. A. Sanders, F. Verhulst, and J. Murdock, *Averaging Methods in Nonlinear Dynamical Systems*, 2nd ed. (Springer-Verlag, New York, 2007).

- [50] D. Wilson and J. Moehlis, An energy-optimal approach for entrainment of uncertain circadian oscillators, *Biophys. J.* **107**, 1744 (2014).
- [51] D. Kirk, *Optimal Control Theory* (Dover Publications, New York, 1998).
- [52] D. Wilson, A. B. Holt, T. I. Netoff, and J. Moehlis, Optimal entrainment of heterogeneous noisy neurons, *Front. Neurosci.* **9**, 192 (2015).
- [53] S. W. Morgan, G. Plank, I. V. Biktasheva, and V. N. Biktashev, Low energy defibrillation in human cardiac tissue: A simulation study, *Biophys. J.* **96**, 1364 (2009).
- [54] E. M. Cherry and S. J. Evans, Properties of two human atrial cell models in tissue: Restitution, memory, propagation, and reentry, *J. Theor. Biol.* **254**, 674 (2008).
- [55] E. G. Tolkacheva, D. G. Schaeffer, D. J. Gauthier, and W. Krassowska, Condition for alternans and stability of the 1:1 response pattern in a “memory” model of paced cardiac dynamics, *Phys. Rev. E* **67**, 031904 (2003).
- [56] K. C. A. Wedgwood, K. K. Lin, R. Thul, and S. Coombes, Phase-amplitude descriptions of neural oscillator models, *J. Math. Neurosci.* **3**, 2 (2013).
- [57] B. Letson and J. E. Rubin, A new frame for an old (phase) portrait: Finding rivers and other flow features in the plane, *SIAM J. Appl. Dyn. Syst.* **17**, 2414 (2018).
- [58] D. Wilson and B. Ermentrout, Greater accuracy and broadened applicability of phase reduction using isostable coordinates, *J. Math. Biol.* **76**, 37 (2018).